

# Flame-made $\text{WO}_3/\text{TiO}_2$ nanoparticles: Relation between surface acidity, structure and photocatalytic activity

Kranthi K. Akurati<sup>a</sup>, Andri Vital<sup>a</sup>, Jean-Philippe Dellemann<sup>a</sup>, Katarzyna Michalow<sup>a</sup>,  
Thomas Graule<sup>a,\*</sup>, Davide Ferri<sup>b</sup>, Alfons Baiker<sup>b</sup>

<sup>a</sup>EMPA, Swiss Federal Laboratories for Materials Testing and Research, Laboratory for High Performance Ceramics,  
Überlandstrasse 129, 8600 Dübendorf, Switzerland

<sup>b</sup>Institute for Chemical and Bioengineering, ETH Zurich, Honggerberg, Wolfgang-Pauli-Strasse 10, 8093 Zurich, Switzerland

Received 27 April 2007; received in revised form 26 September 2007; accepted 28 September 2007

Available online 2 October 2007

## Abstract

$\text{WO}_3/\text{TiO}_2$  composite nanoparticles have been synthesized by dissolving W and Ti precursors in a suitable solvent and spraying into a high temperature acetylene-oxygen flame using a reactive atomizing gas. Particles with controlled W:Ti ratios were produced at various flow rates of precursor solution and the resulting powders were characterized by Brunauer–Emmett–Teller (BET) surface area analysis, X-ray diffraction (XRD), transmission electron microscopy (TEM), Raman and attenuated total reflection infrared (ATR-IR) spectroscopy. Two-dimensional coordinatively unsaturated wolframyl species were well dispersed on the  $\text{TiO}_2$  surface for the samples with equal to or less than 3.6 mol%  $\text{WO}_3$  and contributed to an increase of the surface acidity. Crystalline  $\text{WO}_3$  was formed for samples with >3.6 mol%  $\text{WO}_3$ . Formation of crystalline  $\text{WO}_3$  is attributed to the enhanced rate of condensation of W species with increasing loading of tungsten. Variation of  $\lambda$  (defined as the ratio of the actual oxygen-to-fuel ratio of the reactants to the stoichiometric oxygen-to-fuel ratio) influences the residence time of the particles in the high temperature flame and affects the type of surface species and thereby the resultant acidity. The photocatalytic activity of the composite particles was tested for the degradation of methylene blue (MB) and was compared with that of commercial Degussa P25- $\text{TiO}_2$ . The improved photocatalytic activity of the composite particles is attributed to the increased surface acidity and better charge separation due to the coupling of  $\text{WO}_x$  species and  $\text{TiO}_2$  within the composite nanoparticles.

© 2007 Elsevier B.V. All rights reserved.

**Keywords:** Lewis acids; Acidity; Raman spectroscopy; Photocatalysis; Nanoparticles; Flame spray synthesis; Adsorption;  $\text{WO}_3$ ;  $\text{TiO}_2$

## 1. Introduction

Among the various nanocrystalline photocatalytic materials that have been studied over the last 30 years, research has mainly focused on titanium dioxide (titania,  $\text{TiO}_2$ ) as photocatalyst in diverse areas ranging from water and air treatment to self cleaning surfaces. In the past years  $\text{TiO}_2$  has been modified to suit various applications.  $\text{WO}_3/\text{TiO}_2$  has been successfully tested for selective catalytic reduction (SCR) of  $\text{NO}_x$  in lean exhaust gases

of automobiles to meet the stringent emission standards for both  $\text{NO}_x$  and particulate matter [1–3].  $\text{SiO}_2/\text{TiO}_2$  exhibits super hydrophilic properties which makes it an ideal material for antifogging and self cleaning surfaces such as for window glasses, automobile mirror wind shields, etc. [4]. Numerous papers have appeared on the fundamentals of pure titania systems; the mechanisms of oxidation and the ways to improve its photocatalytic activity (PCA) have been investigated in detail [5–9]. The improvement of the PCA of  $\text{TiO}_2$  has been achieved by coating with noble metals such as Ag [10], Au [11], Pt [12], Pd [13] which can trap the electrons facilitating an effective charge separation. Complementary to metal/ $\text{TiO}_2$  photocatalysts,  $\text{TiO}_2$  has been coupled with other semiconductors such as  $\text{SnO}_2$  [14–17] which can induce effective charge separation by trapping photogenerated electrons. The PCA of metal/metal oxide modified  $\text{TiO}_2$  photocatalysts can be further improved if the metal/metal oxide adsorbs more pollutant along with the function

**Abbreviations:** FSS, flame spray synthesis; PCA, photocatalytic activity; TTIP, titanium tetraisopropoxide; AMT, ammonium metatungstate; DMF, dimethyl formamide; CED, combustion enthalpy density; SSA, specific surface area; MCT, mercury–cadmium–telluride; MB, methylene blue; FWHM, full width at half maximum; HyCOM, hydrothermal crystallization in organic media.

\* Corresponding author. Tel.: +41 44 823 4123; fax: +41 44 823 4150.

E-mail address: [thomas.graule@empa.ch](mailto:thomas.graule@empa.ch) (T. Graule).

of electron trapping. Unfortunately, deposited metal particles only serve as electron trapping agent and are not effective to enhance the adsorption of the pollutants.  $\text{TiO}_2$  coupled with other semiconductors has been reported to perform both the above-mentioned functions. This has been realized by coupling the  $\text{WO}_3$  semiconductor with  $\text{TiO}_2$ . As a basic function,  $\text{WO}_3$  has a suitable conduction band potential to allow the transfer of photogenerated electrons from  $\text{TiO}_2$  facilitating effective charge separation. Additionally, formation of a monolayer of  $\text{WO}_x$  species on  $\text{TiO}_2$  can significantly increase the surface acidity as  $\text{WO}_3$  is 15 times more acidic than  $\text{TiO}_2$  [18]. Because of this increased acidity  $\text{WO}_3/\text{TiO}_2$  can adsorb more hydroxyl groups and simultaneously more organic reactants on its surface. Thus, significant improvement of the PCA has been achieved in comparison to the standard commercial photocatalysts. To date,  $\text{WO}_3/\text{TiO}_2$  has been synthesized by sol–gel [19,20], ball milling [21], incipient wetness impregnation [22,23] and multiple grafting [24]. Thin films of  $\text{WO}_3/\text{TiO}_2$  have also been produced by dip coating [25] and spin coating [26]. Kwon et al. [18] produced  $\text{WO}_3/\text{TiO}_2$  by wetness impregnation method which includes the suspension of pure  $\text{TiO}_2$  powder in a dilute ammonia solution mixed with the required amount of  $\text{H}_2\text{WO}_4$  to adjust the concentration of  $\text{WO}_3$ . The resultant powder was then calcined at  $400^\circ\text{C}$  for 2 h. Acidity increased with increasing amount of  $\text{WO}_3$  and reached a maximum value for a  $\text{WO}_3$  concentration of 3.2 mol%. A further increase in  $\text{WO}_3$  concentration did not have any influence on the acidity of  $\text{WO}_3/\text{TiO}_2$  composite particles. Interestingly, the PCA also followed the same hysteresis as the acidity dependence. Song et al. [23] reported similar results and in addition showed that the stability of the colloidal suspensions of  $\text{WO}_3/\text{TiO}_2$  was enhanced compared to that of  $\text{TiO}_2$  owing to the increased surface acidity. Li et al. [19] synthesized the  $\text{WO}_3/\text{TiO}_2$  by sol–gel process using ethanol solutions of  $\text{Ti}(\text{O}-\text{Bu})_4$  and aqueous solutions of ammonium metatungstate. The resultant amorphous  $\text{WO}_x\text{-TiO}_2$  gel was calcined at 973 K for 2 h to produce crystalline  $\text{WO}_3/\text{TiO}_2$  nanocomposites. The isoelectric point of the resulting 3 mol%  $\text{WO}_3/\text{TiO}_2$  composite was found to be at pH 5.0 compared to pH 6.40 for  $\text{TiO}_2$ . This difference in the isoelectric point can greatly enhance the absorption of organic components on the  $\text{WO}_x/\text{TiO}_2$  photocatalysts.

All the mentioned synthesis routes involve several process in order to improve the crystallinity of the as-synthesized amorphous particles. In this study, the  $\text{WO}_3/\text{TiO}_2$  particles have been synthesized in a single step using the flame spray synthesis (FSS). The concentration of tungsten oxide has been varied in order to produce particles with improved surface acidity and acid strength. As the particle formation takes place at high temperatures in the flame, the resultant powder has a high crystallinity and does not need any further post treatment.

## 2. Experimental procedure

### 2.1. Apparatus

Fig. 1 shows the schematic of the experimental set-up of the FSS. It consists of three syringe pumps to feed the precursor and

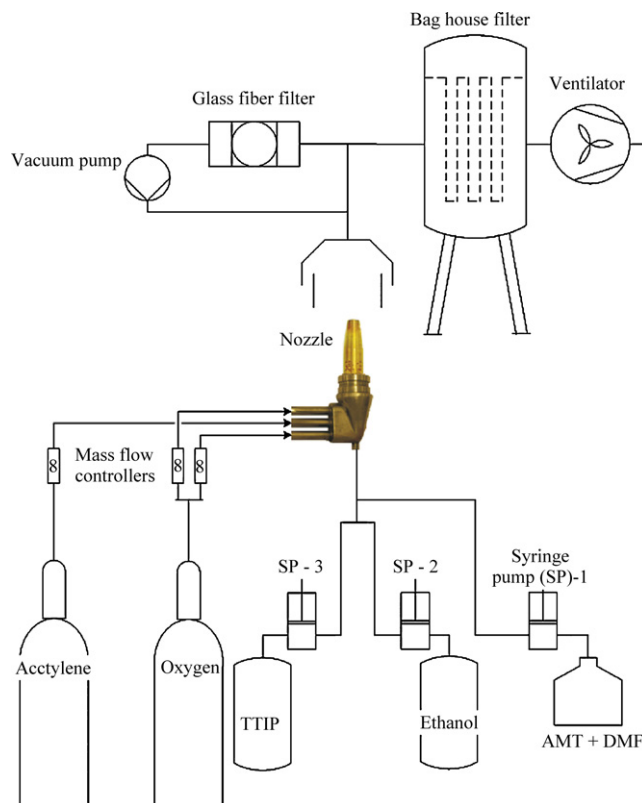


Fig. 1. Experimental set-up for the synthesis of  $\text{WO}_3/\text{TiO}_2$  nanocomposites by flame spray synthesis (FSS) [titanium tetraisopropoxide (TTIP), ammonium metatungstate (AMT), dimethyl formamide (DMF)].

solvent mixtures, an external mixing gas-assisted nozzle and the powder collection unit. Liquid precursor and solvent are stored in separate vessels and both are mixed externally in controlled amounts by adjusting their flow rates with the syringe pumps. The nozzle consists of a central opening (2.8 mm), where a capillary tube (1.05 and 1.59 mm internal and external diameter, respectively) is incorporated and through which the precursor mixture is fed to the flame. The spacing between the capillary tube and central opening is used to feed the atomizing gas (oxygen) that forms a fine spray of the liquid precursor mixture. The spray is ignited by six supporting premixed flamelets produced by  $\text{C}_2\text{H}_2$  (13 l/min) and  $\text{O}_2$  (17 l/min). The openings (1.3 mm) of the supporting flames are located at 3.25 mm from the centre of the nozzle. All gas flow rates are controlled by the mass flow controllers (Bronkhorst HI-TEC). Due to the high exit velocities of the process gases, particles are collected in a bag house filter (Friedli, Switzerland) and representative samples of about 1 g are collected on a glass fiber filter (Type GF50, Schleicher and Schuell, Germany), via a by-pass, using vacuum pumps.

As a precursor source of  $\text{TiO}_2$ , titanium tetraisopropoxide (TTIP,  $\text{Ti}(\text{C}_3\text{H}_7\text{O})_4$ , purity > 99%, VWR International) dissolved in ethanol (99.9% absolute, Fluka AG) was used. Ammonium metatungstate (AMT,  $(\text{NH}_4)_6\text{H}_2\text{W}_{12}\text{O}_{40}(\text{H}_2\text{O})_x$ , 99.9%, ABCR) was used as the precursor source for  $\text{WO}_3$  and was dissolved in dimethyl formamide (DMF,  $\text{C}_3\text{H}_7\text{NO}$ , 99%, ABCR). A 2 M solution of TTIP was prepared and AMT dissolved in different amounts of DMF (0.02 M) was added at a

controlled rate to adjust the tungsten oxide concentration from 1.8 to 9.1 mol%  $\text{WO}_3/\text{TiO}_2$ . The combustion enthalpy density (CED) in this study is defined as the ratio of the total liquid precursor mixture plus acetylene–oxygen (ethanol, TTIP, DMF, AMT,  $\text{C}_2\text{H}_2$  and  $\text{O}_2$ ) combustion enthalpy to the total gas flow in the system. Changing the combustion enthalpy density is associated with the variation of oxygen concentration and combustion stoichiometry ( $\lambda$ ) in the process.  $\lambda$  is defined as the ratio of the actual oxygen-to-fuel ratio of the reactants to the stoichiometric oxygen-to-fuel ratio and was calculated as 10, 4 and 1.3 associated with the combustion enthalpy densities of 9.2, 10.3 and 14.3 kJ/g<sub>gas</sub>, respectively.

## 2.2. Characterization

### 2.2.1. BET, XRD, TEM, Raman and ATR-IR spectroscopy

The specific surface area (SSA) of the product powder was determined from a five-point  $\text{N}_2$  adsorption isotherm obtained from Brunauer–Emmett–Teller (BET) measurements using a Beckman-Coulter SA3100. Prior to BET analysis, the powder samples were degassed at 200 °C for 180 min under flowing  $\text{N}_2$  atmosphere to remove adsorbed  $\text{H}_2\text{O}$  from the surface.

The primary particle size, shape and morphology of the particles were investigated by transmission electron microscopy (TEM). Powder samples were dispersed in isopropanol (purity > 99.5%, Fluka, Switzerland) and a few drops of the dispersion were allowed to dry on carbon-coated copper grids (Plano GmbH, Germany). The TEM analysis was performed on a Philips CM30 electron microscope operating at 200 kV.

X-ray diffraction (XRD) was used for identification of the crystal phases. Diffraction measurements were performed with a PANalytical PW 3040/60 X'Pert PRO instrument using Ni-filtered  $\text{Cu K}\alpha$  radiation of wavelength 1.5418 Å. A  $2\theta$  scan range from 5 to 80°, a scanning step size of 0.01° and a scintillation counter detector was used. Curve fitting and integration was carried out using proprietary software from Philips X'Pert high score plus.

Raman spectra were obtained in backscattering geometry using a Renishaw Ramascope 2000 (Renishaw plc, Gloucestershire, UK) with a spectral resolution of 1  $\text{cm}^{-1}$ . The 633 nm line of the HeNe-laser was focused on the samples through 50× objective of the microscope, the laser beam power on the sample being 0.5 mW. The samples were investigated at room temperature.

Thin particulate films were prepared for the determination of acidity using attenuated total reflection infrared spectroscopy (ATR-IR) from a suspension of the corresponding material (10 mg) in water (1.5 ml, for chromatography). The suspension was deposited on a trapezoidal Ge internal reflection element (IRE) (52 mm × 20 mm × 2 mm, bevels of 45°) and the solvent evaporated in air. After deposition, the coated IRE was mounted within the walls of a home-made infrared cell. ATR-IR measurements were performed by admitting a cyclohexane solution of pyridine (1 mM) saturated with nitrogen over the thin film after stabilization of the IR signal by flowing  $\text{N}_2$ -saturated solvent. Adsorption was followed for 1 h, after which time  $\text{N}_2$ -saturated solvent was again admitted

to the cell to follow desorption for ca. 30 min. Solutions were pumped through the cell by means of a peristaltic pump at ca. 0.6 ml/min flow rate. All measurements were carried out at 30 °C on a Bruker IFS 66 spectrometer equipped with a liquid nitrogen cooled mercury–cadmium–telluride (MCT) detector by accumulating 200 scans at 4  $\text{cm}^{-1}$  resolution. Spectra were corrected by water vapor phase where required. Acidity is given as the ratio between the integrated areas of the signals at 1540 and 1445  $\text{cm}^{-1}$  characteristic of Brønsted and Lewis acid sites, respectively defined as  $C_B/C_L$ . The last spectrum recorded during desorption was used for integration. Signal integration was performed with the OPUS vs. 3.1 software.

The PCA of the as-synthesized powders was evaluated by the degradation of the standard pollutant, methylene blue (MB). Details of the photochemical reactor have been reported elsewhere [15]. Samples for UV–vis spectroscopy were filtered through 0.2  $\mu\text{m}$  Whatman Anotop 10 membrane filters to remove the photocatalyst particles before analysis. Calibration of the absorbance at 660 nm against MB concentration (Lambert-Beer) was carried out for quantification of the PCA.

## 3. Results and discussion

### 3.1. Physical properties of $\text{WO}_3/\text{TiO}_2$

Pure  $\text{TiO}_2$  and  $\text{WO}_3$  appear physically in white and yellow color, respectively. But the color of the  $\text{WO}_3/\text{TiO}_2$  powders synthesized at  $\lambda$  of 10 are light yellow and those produced at  $\lambda$  of 4 and 1.3 are pale blue in color. On the other hand, particles synthesized with 9.1 mol%  $\text{WO}_3/\text{TiO}_2$  at  $\lambda$  4 and 1.3 have vivid blue color. Yellow color is indicative of stoichiometric  $\text{WO}_3$  in which W has valency of 6<sup>+</sup>. The appearance of blue color is evidence for the presence of  $\text{W}^{6+}$  and  $\text{W}^{5+}$  in equilibrium and might have formed due to the decreasing oxidizing potential of the flame with decreasing value of  $\lambda$ . With increasing concentration of tungsten, its complete oxidation is inhibited because of the shorter residence time of the particles in the flame due to increased total precursor flow rate.

### 3.2. $\text{N}_2$ physisorption measurement (BET)

Fig. 2 shows the SSA of the  $\text{WO}_3/\text{TiO}_2$  nanocomposites synthesized as a function of CED of the process. Irrespective of the concentration of  $\text{WO}_3$ , the SSA of the  $\text{WO}_3/\text{TiO}_2$  particles decreased with increasing CED. The temperature of the flame increases with the increasing CED [27]. An increase in the flame temperature and combustion enthalpy density enhances the sintering rate of the particles facilitating them to grow to large sizes and concomitantly decrease the SSA. This is similar to the conventional flame aerosol process where the surface area of the particles decreases with increasing temperature as reported by several authors [28,29]. It is also in agreement with other FSP studies reported earlier [30,31].

Addition of  $\text{WO}_3$  increases the SSA of the resultant  $\text{WO}_3/\text{TiO}_2$  particles in comparison to pure  $\text{TiO}_2$ . Crystalline  $\text{WO}_3$  particles did not form at low concentrations (<3.6 mol%) of tungsten (will be shown in Section 3.5), instead, amorphous  $\text{WO}_x$

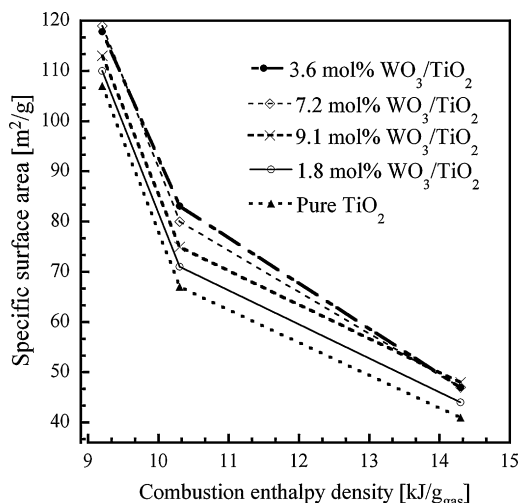


Fig. 2. Specific surface area (SSA) of the  $\text{WO}_3/\text{TiO}_2$  nanocomposites synthesized with various concentrations of  $\text{WO}_3$ .

species deposited on the surface of  $\text{TiO}_2$  particles. Growth of the  $\text{TiO}_2$  particles takes place in the flame by coagulation and coalescence mechanisms. Formation of the thin layer of  $\text{WO}_x$  species, at low concentrations of tungsten, partially prevents the growth between the  $\text{TiO}_2$  particles thus leading to increased SSA of the resultant  $\text{WO}_x/\text{TiO}_2$  particles. Crystalline  $\text{WO}_3$  particles tend to form with increasing tungsten concentrations and the SSA of the resulting  $\text{WO}_3/\text{TiO}_2$  particles decreases. This observed decrease in the SSA is solely due to the higher density of tungsten in relation to titanium as little or no variation is observed in the  $d_{\text{BET}}$  values of the respective powders.

### 3.3. X-ray diffraction

Fig. 3 shows the XRD patterns of the 3.6 mol%  $\text{WO}_3/\text{TiO}_2$  particles as a function of the CED. Predominantly, the anatase phase is observed in all the samples with a minute fraction of

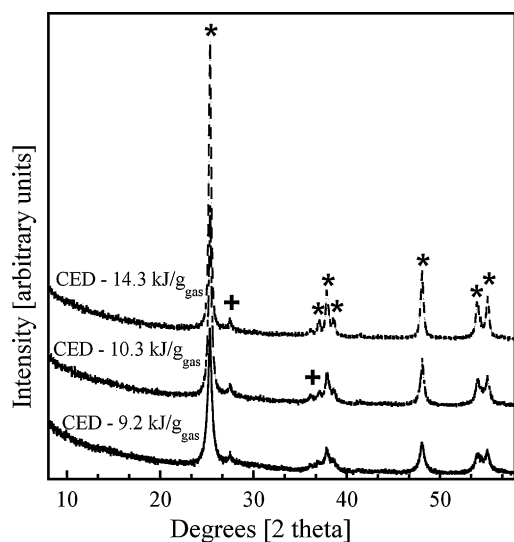


Fig. 3. XRD patterns of 3.6 mol%  $\text{WO}_3/\text{TiO}_2$  nanocomposites synthesized with increasing CED values. Symbols (★) and (+) indicate the anatase and rutile phases, respectively.

rutile. The main reflection of anatase is observed at  $2\theta = 25.4^\circ$ . The full width at half maximum (FWHM) of the reflection, which is the characteristic of the crystallite size of the corresponding phase, decreases with increasing CED and corresponds to the increase of the crystallite size. This agrees well with the BET results which showed decrease of the SSA with increase in the CED value. Few authors reported that the addition of tungsten increases the thermal stability of  $\text{TiO}_2$  and stabilizes the anatase phase [32,33]. However, no reflections corresponding to the formation of mixed oxides of  $\text{TiO}_2\text{--WO}_3$  or pure  $\text{WO}_3$  are seen in the XRD patterns. So, the formation of the  $\text{TiO}_2$  anatase phase is associated with the flame spray process parameters as pure  $\text{TiO}_2$  produced under similar conditions also showed predominantly anatase phase. The addition of  $\text{WO}_3$  did not induce any significant change in the phase composition. The lack of reflections corresponding to  $\text{WO}_3$  reveals that it is present either in the form of highly dispersed  $\text{WO}_x$  clusters or as an amorphous layer on  $\text{TiO}_2$  as reported by several authors [18,21] or the concentration of  $\text{WO}_3$  is too low for the XRD to reveal.

In contrast, reflections corresponding to crystalline  $\text{WO}_3$  are seen in the XRD pattern of nanocomposites synthesized at 9.1 mol%  $\text{WO}_3/\text{TiO}_2$  (Fig. 4). Engweiler et al. [24] studied the formation of  $\text{WO}_3/\text{TiO}_2$  composites via multiple grafting procedure by step-wise increase of the concentration of  $\text{WO}_x$  species and concluded that a highly dispersed amorphous monolayer of  $\text{WO}_x$  species forms on  $\text{TiO}_2$  at low tungsten loading. When the tungsten concentration exceeds over that required for  $\text{WO}_x$  monolayer formation crystalline  $\text{WO}_3$  will form. Similar observations have been made in the present study with the increased concentration of tungsten oxide.

### 3.4. Transmission electron microscopy

Fig. 5(a and b) shows the TEM images of the 3.6 mol%  $\text{WO}_3/\text{TiO}_2$  produced at CED of 9.2 and 14.3 kJ/g\_gas respectively. Particles are spherical in morphology and non-aggregated with a

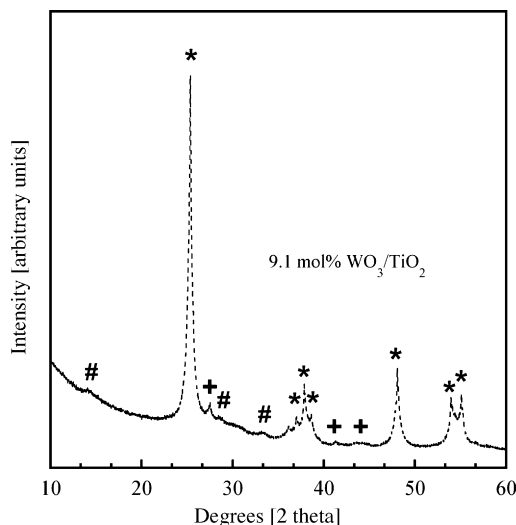


Fig. 4. XRD pattern of the 9.1 mol%  $\text{WO}_3/\text{TiO}_2$  nanocomposites synthesized with CED of 9.4 kJ/g\_gas. Symbols (★) and (+) indicate the anatase and rutile phases, respectively. The symbol (#) indicates the crystalline phase of  $\text{WO}_3$ .



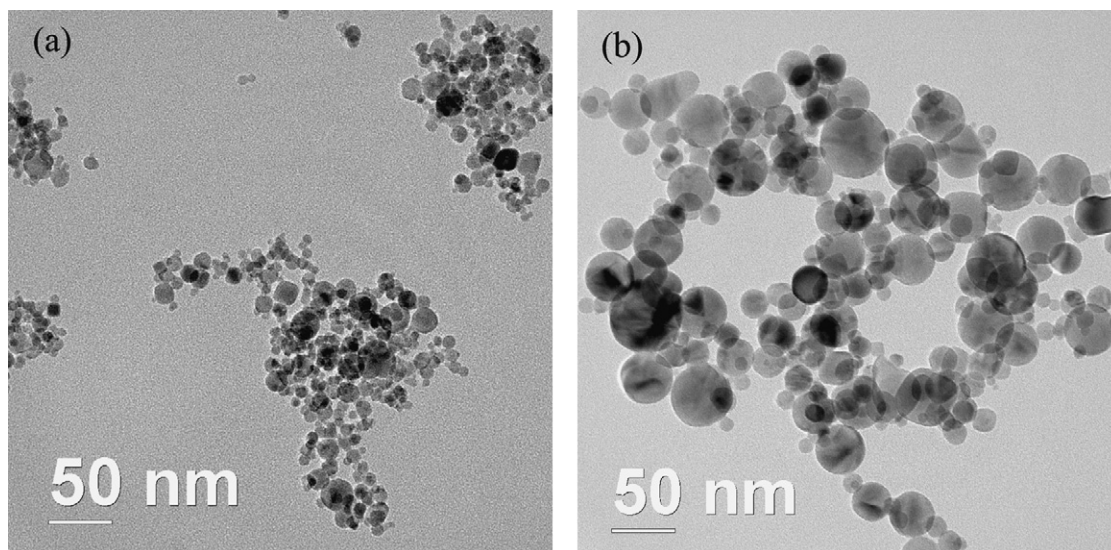


Fig. 5. TEM images of the 3.6 mol%  $\text{WO}_3/\text{TiO}_2$  nanocomposites synthesized at the CED of (a) 9.2 and (b) 14.3  $\text{kJ/g}_{\text{gas}}$ .

size ranging from 5 to 20 nm and 10 to 50 nm for the CED value of 9.2 and 14.3  $\text{kJ/g}_{\text{gas}}$ , respectively.

Synthesis of inhomogeneous and hollow particles via FSP has been reported by several authors [31,34,35]. Jossen et al. [36] made a systematic study and proposed that either of the following process parameters have to be met to produce homogeneous and solid particles:

- (1) The combustion enthalpy density of the flame should be  $>4.7 \text{ kJ/g}_{\text{gas}}$ .
- (2) The ratio of the boiling point of the solvent ( $T_{\text{bp}}$ ) to the decomposition/melting point of the dissolved precursor ( $T_{\text{d/mp}}$ ) should be  $>1$ .

If the combustion enthalpy density is  $<4.7 \text{ kJ/g}_{\text{gas}}$ , then the ratio of  $T_{\text{bp}}/T_{\text{d/mp}}$  should be  $>1$  and vice versa.

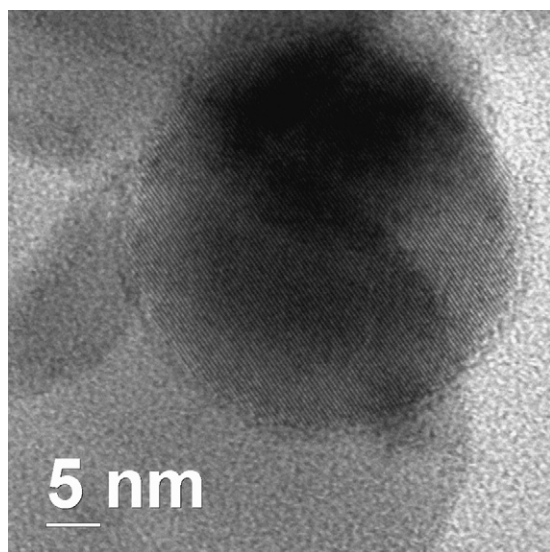


Fig. 6. High resolution image of the 3.6 mol%  $\text{WO}_3/\text{TiO}_2$  nanocomposite synthesized at the CED of 14.3  $\text{kJ/g}_{\text{gas}}$ . Lattice spacing indicative of (1 0 1) plane of anatase.

Homogeneous and solid particles are produced in the present study (Figs. 5 and 6). The combustion enthalpy density of the flame with  $\lambda$  values of 10, 4 and 1.3 is 9.2, 10.3 and 14.3  $\text{kJ/g}_{\text{gas}}$ , respectively, and the  $T_{\text{bp}}$  (ethanol 78.3  $^{\circ}\text{C}$ )/ $T_{\text{d/mp}}$  (TTIP 232  $^{\circ}\text{C}$ ) ratio is  $<1$ . Jossen et al. [36] did not consider the enthalpy of  $\text{CH}_4$  and  $\text{O}_2$  combustion in their calculation of the total combustion enthalpy density of the flame. This may have to do with the low flow rate of  $\text{CH}_4$  (0.5 l/min) and  $\text{O}_2$  (2 l/min) used in their study. In the present study higher flow rates of  $\text{C}_2\text{H}_2$  (13 l/min) and  $\text{O}_2$  (17 l/min) are used whose combustion enthalpy rate ( $-775.5$  against  $-18.9 \text{ kJ/min}$  in Jossen's study [36]) cannot be neglected. Though there is a difference in the way the combustion enthalpy density is calculated between the present study and Jossen et al. [36], the criterion of having combustion enthalpy density  $>4.7 \text{ kJ/g}_{\text{gas}}$  to produce solid particles is well supported.

The high resolution image (Fig. 6) of the 3.6 mol%  $\text{WO}_3/\text{TiO}_2$  particles shows uniform lattice fringes whose spacing corresponds to (1 0 1) planes of anatase phase of  $\text{TiO}_2$  and no individual clusters/particles of  $\text{WO}_3$  are seen on the surface of  $\text{TiO}_2$ . This indicates that the tungsten oxide species might have covered the surface of  $\text{TiO}_2$  particles as amorphous layer. This is consistent with the results obtained from the Raman spectroscopy (next section) showing the existence of amorphous  $\text{WO}_x$  and agrees well with previous reports [18,23].

### 3.5. Raman spectroscopy

The Raman spectrum of the pure  $\text{WO}_3$  powder (Fig. 7) shows sharp signals at 280, 313, 688–717, 817  $\text{cm}^{-1}$  and a very weak peak at 950  $\text{cm}^{-1}$ . The signals at 280 and 313  $\text{cm}^{-1}$  correspond to O–W–O bending modes of bridging oxygen, and the signals at 817  $\text{cm}^{-1}$  and in the 688–717  $\text{cm}^{-1}$  range are the corresponding stretching modes. The weak signal at 950  $\text{cm}^{-1}$  corresponds to the terminal W=O bond which forms on tungsten ions with low coordination numbers as in amorphous  $\text{WO}_3$  [37]. Rampaul et al. [25] reported the Raman spectrum of sol-gel synthesized  $\text{WO}_3$  films and observed a prominent signal

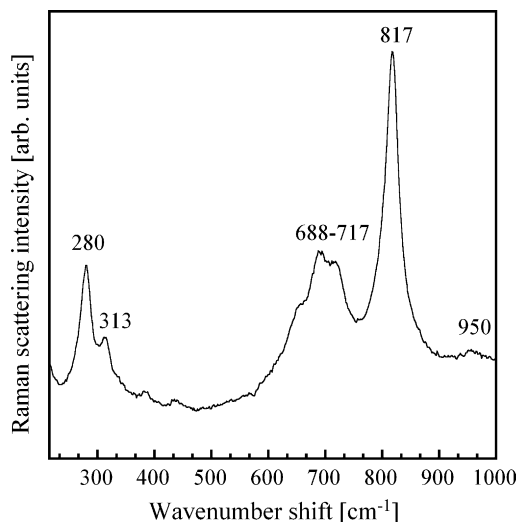


Fig. 7. Raman spectrum of the as-synthesized  $\text{WO}_3$  nanopowder. Wavenumber-shift is shown on top of the corresponding peak.

at  $924\text{ cm}^{-1}$  corresponding to amorphous  $\text{WO}_3$ , whereas the Raman peaks corresponding to crystalline  $\text{WO}_3$  at 304, 717 and  $807\text{ cm}^{-1}$  appeared less intense. This reveals the less crystalline nature of the sol–gel derived materials unless they are calcined at a sufficiently high temperature. Habazaki et al. [38] reported the Raman spectra of annealed electrodeposited  $\text{WO}_3$  films at several temperatures. The intensity of the Raman peaks corresponding to crystalline  $\text{WO}_3$  increases with annealing temperature and the most intense peak is positioned at  $817\text{ cm}^{-1}$  which agrees well with the present study.

Fig. 8 shows the Raman spectra of  $\text{WO}_3/\text{TiO}_2$  samples in the  $750\text{--}1200\text{ cm}^{-1}$  spectral range. The spectrum of the 1.8 mol%  $\text{WO}_3/\text{TiO}_2$  sample (Fig. 8A) shows a relatively weak band centred at  $969\text{ cm}^{-1}$  which can be assigned to the  $\text{W}=\text{O}$

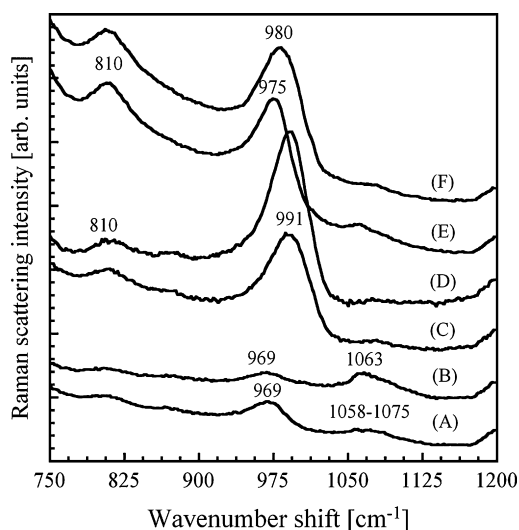
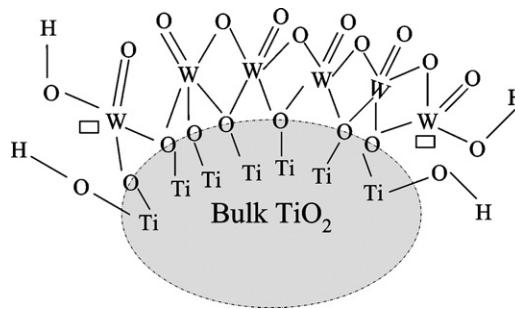


Fig. 8. Raman spectra of the  $\text{WO}_3/\text{TiO}_2$  nanoparticles synthesized at various concentrations of  $\text{WO}_3$  at  $\lambda = 1.3$  and 10. The measurements were performed with the narrow wavenumber shift to resolve weak peaks of  $\text{WO}_x$  species. Spectra A–D correspond to  $\text{WO}_3/\text{TiO}_2$  particles synthesized at 1.8, 3.6, 7.2 and 9.1 mol%  $\text{WO}_3$ , respectively at  $\lambda = 10$ , while spectra E and F correspond to  $\text{WO}_3/\text{TiO}_2$  particles synthesized at 1.8 and 3.6 mol%  $\text{WO}_3$ , respectively, at  $\lambda = 1.3$ .

stretching vibration of surface wolframyl species [39]. This two-dimensional surface tungsten oxide species exists in  $\text{WO}_5$  units at this low W concentration and the signal corresponding to the  $\text{WO}_x$  species in tetrahedral coordination is revealed by the presence of the broad band ranging from  $1058$  to  $1075\text{ cm}^{-1}$  [40]. The presence of the very weak signal close to  $810\text{ cm}^{-1}$  suggests that only a very small fraction of the added W contributed to the formation of crystalline  $\text{WO}_3$ . The Raman stretching frequency of the surface tungsten oxide species for a given support oxide ( $\text{TiO}_2$  in this study) depends on the amount of W loading and on the nature of W–O coordination (W–O bond order). Since the high frequency of a given signal reflects a high bond order, i.e. shortest W–O bond in the tungsten oxide species, signals characteristic of tetrahedrally coordinated tungsten oxide species ( $\text{WO}_4$ ) appear at higher wavenumber than octahedral  $\text{WO}_6$  species due to the higher bond order of the former [40]. Additionally, the Raman scattering cross-section of tetrahedrally coordinated  $\text{WO}_x$  species is much higher than that of the octahedrally coordinated type. Hence the presence of tetrahedrally coordinated  $\text{WO}_x$  species can be easily revealed even when present in minute amounts. Based on these considerations, a schematic of surface tungsten oxide species on the  $\text{TiO}_2$  support is shown in Scheme 1.

Characterization of  $\text{Ti}(\text{WO}_4)_2$  type tungsten oxide species by Raman spectroscopy has not been reported in  $\text{WO}_3/\text{TiO}_2$  literature so far. Bond et al. [41] reported unassigned Raman signals around  $1000\text{ cm}^{-1}$  after increasing the surface area of  $\text{TiO}_2$  and concluded that several different surface tungsten oxide species can be formed on high surface area supports compared to low surface area supports. The high SSA of the  $\text{WO}_3/\text{TiO}_2$  particles reported in this study might be responsible for the  $\text{WO}_4$  groups on  $\text{TiO}_2$  surface. For the 3.6 mol%  $\text{WO}_3/\text{TiO}_2$  particles, the characteristic signal of  $\text{WO}_4$  slightly narrowed and showed a maximum at  $1063\text{ cm}^{-1}$ . No features of crystalline  $\text{WO}_3$  are observed indicating that even at 3.6 mol%  $\text{WO}_3$  the surface of  $\text{TiO}_2$  is populated by two-dimensional tungsten oxide species.

Significant changes occur in the position of the Raman signals with increasing the concentration of  $\text{WO}_3$  to 7.2 mol% (Fig. 8C) which do not change at 9.1 mol%  $\text{WO}_3$  (Fig. 8D). The signal close to  $1060\text{ cm}^{-1}$  vanishes and a new one appears at  $810\text{ cm}^{-1}$  representative of the O–W–O stretching mode of three-dimensional crystalline  $\text{WO}_3$ . In addition, the signal at



Scheme 1. Evolution of  $\text{WO}_x$  species and acidity on  $\text{TiO}_2$  at low concentrations of  $\text{WO}_3$ . Rectangles represent the coordinatively unsaturated terminal groups responsible for the Brønsted acidity of  $\text{WO}_3/\text{TiO}_2$  powder.

969  $\text{cm}^{-1}$  observed in the 1.8 and 3.6 mol% samples is shifted to 991  $\text{cm}^{-1}$  indicating the presence of octahedral  $\text{WO}_6$  groups. Vuurman et al. [37] reported a signal at 935  $\text{cm}^{-1}$  for 1 wt%  $\text{WO}_3/\text{TiO}_2$  that shifted to  $\sim 965 \text{ cm}^{-1}$  with increasing the W concentration to 8 wt% corresponding to the formation of a layer of  $\text{WO}_3$ . Chan et al. [42] reported a signal at 942  $\text{cm}^{-1}$  for 1 wt%  $\text{WO}_3/\text{TiO}_2$  which shifted to  $\sim 972 \text{ cm}^{-1}$  at 10 wt%  $\text{WO}_3$ . Further similar observations have been made for  $\text{WO}_x$  on alumina [43] and vanadia on titania where the Raman signals shifted with coverage of the surface oxide species from  $\sim 965$  to 1000 and from  $\sim 940$  to 1000  $\text{cm}^{-1}$ , respectively. The observed shift with increasing  $\text{WO}_3$  concentration was attributed to the change of coordination in W species to octahedral. Hence, the tungsten oxide species exist in octahedral coordination at high W concentration, which is supported by the absence of the characteristic signals of  $\text{WO}_4$  species. Crystalline  $\text{WO}_3$  particles also formed with increasing W concentration due to an increased degree of condensation of W species.

The Raman spectra of the  $\text{WO}_3/\text{TiO}_2$  particles produced at  $\lambda = 1.3$  exhibit a significant difference compared to the particles synthesized at  $\lambda = 10$  (Fig. 8E and F). For 1.8 mol%  $\text{WO}_3/\text{TiO}_2$  particles (Fig. 8E), a signal is observed at 975  $\text{cm}^{-1}$  indicative of W=O stretching vibration in surface wolframyl species in which W exists in  $\text{WO}_5$  units. A strong signal at 810  $\text{cm}^{-1}$  reveals the presence of a significant fraction of three-dimensional crystalline  $\text{WO}_3$  that was absent in the particles synthesized at  $\lambda = 10$ . Decreasing  $\lambda$  increases the residence time of the particles in the flame and concomitantly decreases the specific surface area (44  $\text{m}^2/\text{g}$  at  $\lambda = 1.3$  and 110  $\text{m}^2/\text{g}$  at  $\lambda = 10$ ). Decreasing the SSA of the particles results in less surface available for the dispersion of tungsten oxide species. This leads to a decreased spacing between the two-dimensional surface tungsten oxide species, which then tend to oligomerize to form three-dimensional crystalline  $\text{WO}_3$  particles aided by the increased residence time in the high temperature flame. The weak signal at 1050  $\text{cm}^{-1}$  indicates that a very small fraction of tetrahedrally coordinated tungsten oxide is also present. A coverage dependent shift (from 975 to 980  $\text{cm}^{-1}$ ) of the signal is observed with increasing  $\text{WO}_3$  concentration from 1.8 to 3.6 mol%.

### 3.6. Surface acidity

The ATR-IR spectra of pyridine adsorbed on pure  $\text{WO}_3$ ,  $\text{TiO}_2$  and on  $\text{WO}_3/\text{TiO}_2$  composite particles are shown in Fig. 9. The signals at 1445, 1490 and 1540  $\text{cm}^{-1}$  are attributed to pyridine adsorbed on Lewis acid sites, on both Lewis and Brønsted sites, and Brønsted acid sites, respectively. The signal at 1570  $\text{cm}^{-1}$  represents physically adsorbed pyridine, whereas hydrogen bonded pyridine with surface OH groups is revealed by the characteristic signals at 1600 and 1625  $\text{cm}^{-1}$ . Surface acidity of pure anatase is only of the Lewis type and no signals corresponding to Brønsted acid sites were detected. This is in agreement with Morterra et al. [44] reporting Brønsted acidity for sulphated  $\text{TiO}_2$  but only Lewis acidity for  $\text{TiO}_2$ .

Incorporation of 1.8 mol%  $\text{WO}_3$  results in a significant increase of Lewis acidity and in the appearance of Brønsted

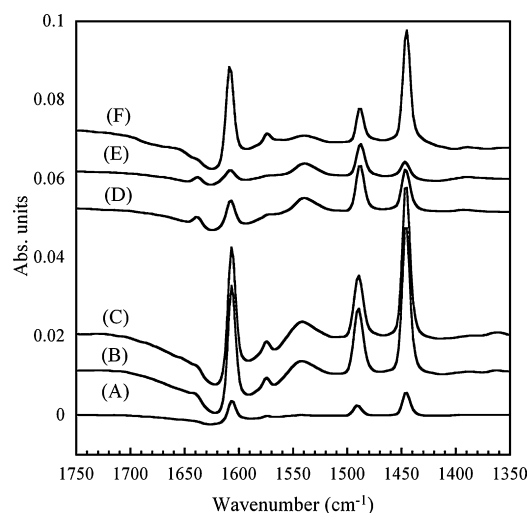


Fig. 9. ATR-IR spectra of  $\text{WO}_3/\text{TiO}_2$  nanoparticles synthesized at  $\lambda = 10$  and comparison with  $\text{TiO}_2$  (spectrum A) and  $\text{WO}_3$  (spectrum F). Spectra B–E correspond to  $\text{WO}_3/\text{TiO}_2$  particles synthesized at 1.8, 3.6, 7.2 and 9.1 mol%  $\text{WO}_3$ , respectively.

acid sites, whereas increasing the  $\text{WO}_3$  concentration to 3.6 mol% causes only a slight increase in the Brønsted acidity. Hence, both types of acidity co-exist on the  $\text{WO}_3/\text{TiO}_2$  particles. Raman spectroscopy revealed that at relatively low loadings of  $\text{WO}_3$ , wolframyl species containing W=O bonds are the dominant and partially covering the  $\text{TiO}_2$  surface. These surface tetrahedral wolframyl species are coordinatively unsaturated and act as strong Lewis acid sites [45,46]. Hilbrig et al. [47] reported by XANES study that the tungsten anchored to the surface as branched chains of  $\text{WO}_5$  and these chains are terminated by  $\text{WO}_4$  units, the relative proportion of which increases with loading before W attains its usual hexavalent coordination. The Brønsted acidity may arise from the coordinatively unsaturated terminal groups in contact with  $\text{TiO}_2$  (Scheme 1), and grow in number with increasing W-concentration.

Although it is not meaningful to quantify surface acidity solely from infrared spectra obtained from pyridine adsorption, since the  $\text{WO}_3/\text{TiO}_2$  samples produced with  $\lambda = 10$  exhibit comparable SSA (ca. 110  $\text{m}^2/\text{g}$ ) and so do the samples produced at  $\lambda = 1.3$  we can risk a comparison between samples produced at the same  $\lambda$  using both the  $C_B/C_L$  ratio and a qualitative comparison between ATR-IR spectra.

The  $C_B/C_L$  ratio depicted in Fig. 10 suggests that the Brønsted acidity steadily increases with W-concentration and drops dramatically in  $\text{WO}_3$ . This is also qualitatively demonstrated by intensity of the signal at 1540  $\text{cm}^{-1}$  which is clearly inferior in  $\text{WO}_3$  than in the  $\text{WO}_3/\text{TiO}_2$  samples. This reveals that the interface which develops with W-content develops additional Brønsted acidity to  $\text{WO}_3$  that grows until 9.1 mol% and then drops for bulk  $\text{WO}_3$ .

Fig. 10 shows an abrupt increase in the  $C_B/C_L$  ratio from 3.6 to 7.2 mol% W, which is interpreted as a dramatic decrease in the Lewis acidity and with the formation of a three-dimensional octahedral  $\text{WO}_3$ -like phase as demonstrated by Raman spectroscopy rather than to a further increase of the Brønsted



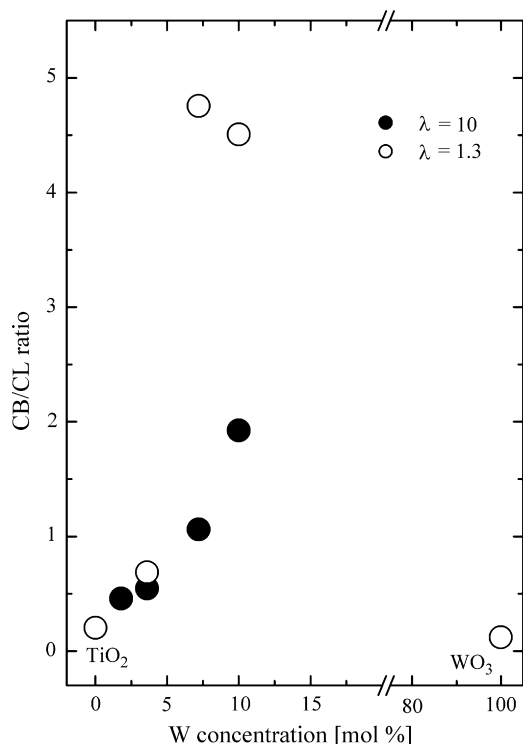


Fig. 10. Ratio of the integrated area of the signals at 1540 ( $C_B$ ) and 1445  $\text{cm}^{-1}$  ( $C_L$ ) characteristic of Brønsted and Lewis acid sites, respectively, as a function of W-loading for two different lambda values.

acidity. The decrease in the intensity of the signal at 1445  $\text{cm}^{-1}$  (Lewis acid sites) in Fig. 9 when increasing the W-content to 7.2 mol% likely supports this interpretation. The surface of the WO<sub>3</sub>-like phase is populated predominantly by coordinatively saturated species. The higher  $C_B/C_L$  ratio in the 7.2 mol% sample compared to the 1.8 and 3.6 mol% samples has then to be attributed almost uniquely to a change in the Lewis acidity rather than to Brønsted acidity. This is confirmed by the results in Fig. 10 showing that the Brønsted acidity of the WO<sub>3</sub>/TiO<sub>2</sub> particles decreases with increasing  $\lambda$ , which is again in agreement with the Raman spectra.

### 3.7. Photocatalytic activity

Fig. 11 shows the kinetics of disappearance of MB for pure TiO<sub>2</sub> (Degussa P25) and 3.6 mol% WO<sub>3</sub>/TiO<sub>2</sub> powder synthesized at various values of  $\lambda$ . No detectable degradation of MB occurs without TiO<sub>2</sub> or with UV radiation alone. It is obvious from Fig. 11 that the powder (3.6 mol% WO<sub>3</sub>/TiO<sub>2</sub>) synthesized at  $\lambda = 10$  shows improved PCA compared to P25-TiO<sub>2</sub>.

The 3.6 mol% WO<sub>3</sub>/TiO<sub>2</sub> powder synthesized in the present study at  $\lambda$  value of 10 has a large SSA of 118  $\text{m}^2/\text{g}$ , but the associated crystallinity is much less than P25-TiO<sub>2</sub>. Despite this, it shows better PCA than P25-TiO<sub>2</sub> which cannot be explained like the strategy (large surface area associated with high crystallinity) followed to synthesize hydrothermal crystallization in organic media (HyCOM) TiO<sub>2</sub> powder [48], which shows higher PCA than P25-TiO<sub>2</sub>. The improved PCA can be

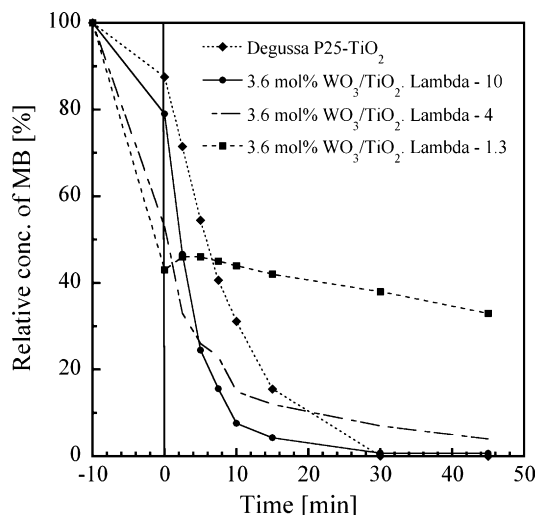


Fig. 11. Comparison of the PCA of the 3.6 mol% WO<sub>3</sub>/TiO<sub>2</sub> nanocomposites and Degussa P25-TiO<sub>2</sub>. Negative time (–10 min) indicates the period of adsorption of MB in the dark (without illumination).

understood by considering the Langmuir-Hinshelwood kinetic scheme, where the rate of photocatalytic degradation is enhanced when the apparent reaction rate constant and the equilibrium adsorption constant is increased [49]. The apparent reaction rate constant depends on how well the photogenerated charge carriers separate without their recombination. Rothenberger et al. [50] studied the dynamics of charge carrier trapping and recombination with picosecond and nanosecond laser photolysis in an aqueous solution and reported that trapping of conduction band electrons and valence band holes occurs in 30 ps and 250 ns, respectively. Hence, effective electron trapping has to be carried out to prevent recombination with the hole. The rate-determining step for degradation in the slurry based photocatalytic reactors is proved to be the trapping of electrons by oxygen [51]. In a typical TiO<sub>2</sub> particulate system, lots of probable functions are involved for the circulating oxygen to get reduced by the photogenerated electron. Due to this oxygen reacts very slowly with the photogenerated electrons leading to their accumulation and probable recombination with holes that decrease the photocatalytic activity. On the other hand, incorporation of an electron trapping agent on the surface of TiO<sub>2</sub> will trap the electrons much faster than the oxygen and prevent the recombination with the hole. The 3.6 mol% WO<sub>3</sub>/TiO<sub>2</sub> composite particles produced in this study at  $\lambda = 10$  have a surface layer of WO<sub>x</sub> species in which the valence state of W is 6<sup>+</sup>. When pure TiO<sub>2</sub> is illuminated under UV light, the absorption is associated with the O<sup>2-</sup>  $\rightarrow$  Ti<sup>4+</sup> charge transfer transitions corresponding to the excitation of electrons from the valence band (having the O 2p character) to the conduction band (having the Ti 3d character). Gutiérrez-Alejandre et al. [46] performed the UV–vis absorption measurements on pure TiO<sub>2</sub> and WO<sub>3</sub>/TiO<sub>2</sub> particles and found no differences in absorption behavior, indicating that 5d orbitals of W lie into the Ti 3d conduction band so that O<sup>2-</sup>  $\rightarrow$  W<sup>6+</sup> and O<sup>2-</sup>  $\rightarrow$  Ti<sup>4+</sup> charge transfer transitions are superimposed. Hence, when WO<sub>x</sub>/TiO<sub>2</sub> is illuminated, absorption is associated with the



$O^{2-} \rightarrow W^{6+}$  transition and the electron is trapped by  $W^{6+}$ . Circulating oxygen, as a passive electron trapping agent, is still needed, in spite of the presence of  $WO_x$  species as an active electron trap.  $W^{6+}$  easily reduces to  $W^{5+}$  by electron trapping and the presence of the  $W^{6+}-W^{5+}$  pair alters the physical and chemical properties of the reduced  $WO_x$  species which has a negative influence on the PCA [22]. The presence of the oxygen oxidizes the  $W^{5+}$  back to  $W^{6+}$  which can further trap the electron. In this way,  $WO_x$  deposited on the  $TiO_2$  surface acts as an electron acceptor in the  $WO_3/TiO_2$  system to increase the apparent rate constant.

The equilibrium adsorption constant is related to the surface characteristics of the photocatalyst, i.e. surface area and affinity of the photocatalyst surface to the pollutant. We have demonstrated that the surface of  $WO_3/TiO_2$  is more acidic than that of  $TiO_2$ . The increased acidity generates a higher affinity of  $WO_3/TiO_2$  for species with unpaired electrons. Because of this, this material can absorb more  $OH^-$  or  $H_2O$ , which is prerequisite for  $OH$  radical formation necessary for photooxidation reactions. Therefore, the combination of improved charge separation (increased apparent rate constant) and affinity to adsorb the pollutant (increased equilibrium adsorption constant) are responsible for the improved PCA of 3.6 mol%  $WO_3/TiO_2$ .

It can be seen from Fig. 11 that the PCA of the 3.6 mol%  $WO_3/TiO_2$  composites decreases with decreasing  $\lambda$ . As mentioned in Section 3.1, the color of the powder turns to blue with decreasing  $\lambda$ , revealing that tungsten has been partially reduced from  $W^{6+}$  to  $W^{5+}$ . Reduced  $WO_3$  has oxygen vacancies that act as electron donors and are not able to trap electrons due to the repulsive forces. The increase of electron density in reduced  $WO_3$  enhances the electron–hole recombination rate which is detrimental to the PCA. However, high electron density associated with the oxygen vacancies of reduced  $WO_3$  gives rise to negative charge which enhances adsorption of the cationic MB dye. As a consequence, the negative effect of inability to trap electrons by reduced  $W$  species dominates the positive influence of adsorption leading to the reduction of the PCA.

MB degradation kinetics of pure  $WO_3$  and  $WO_3/TiO_2$  particles with increasing concentration of  $WO_3$  is shown in Fig. 12. 3.6 mol%  $WO_3/TiO_2$  shows improved activity compared to 1.8 mol%  $WO_3/TiO_2$  because of the increased acidity of the former.  $TiO_2$  with 7.2 mol%  $WO_3$  shows much stronger adsorption characteristics due to the presence of separate  $WO_3$  particles that have high acid strength, a trend similar to that of pure  $WO_3$ . Several authors have reported the importance of the acid site strength alongside with the amount of acid sites for the catalytic activity. Yamanaka and Tanabe [52] studied the acid site strength of various metal oxides and reported that  $WO_3$  possesses significantly higher acid strength than  $TiO_2$ . Though the amount of acid sites is less in 7.2 mol%  $WO_3/TiO_2$ , the acid site strength is much higher due to the presence of crystalline  $WO_3$  which accounts for the increased adsorption of MB. Due to this high adsorption, the activity of the 7.2 mol%  $WO_3/TiO_2$  nanocomposites is almost negligible. An improvement of the PCA with optimum amounts of  $WO_3$

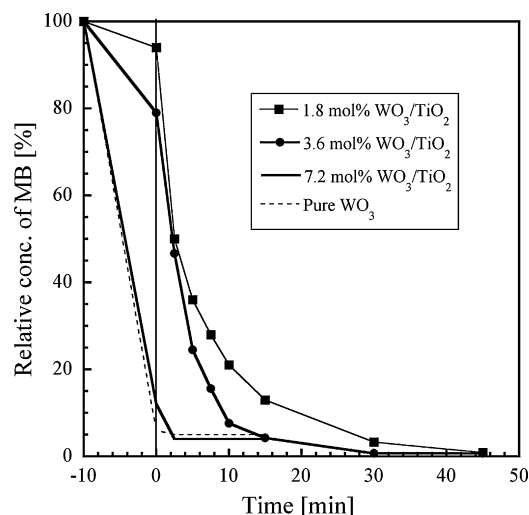


Fig. 12. PCA of the  $WO_3/TiO_2$  nanoparticles with increasing concentration of  $WO_3$ . Nearly complete adsorption of MB has been observed in the dark for the sample containing  $\geq 7.2$  mol%  $WO_3$ .

has been reported by several authors. Li et al. [19] reported the synthesis of  $WO_3/TiO_2$  by sol–gel method and at 1 mol%  $WO_3$  maximum improvement of the PCA is observed. In contrast Kwon et al. [18] reported the synthesis of  $WO_3/TiO_2$  by wetness impregnation method and maximum improvement of PCA was found at 3 mol%  $WO_3$  and agrees well with the results of the present study.

#### 4. Conclusions

$WO_3/TiO_2$  nanoparticles with controlled amount of  $W$ -doping have been successfully synthesized by flame spray synthesis at designated oxygen-to-fuel ratios  $\lambda$ . The coordination of  $WO_x$  species changed from tetrahedral to octahedral with increasing concentration of  $WO_3$ . At a  $WO_3$  concentration of  $<3.6$  mol% and high  $\lambda$  amorphous  $WO_x$  species formed on the surface of  $W$ -doped  $TiO_2$  substrate particles. This surface layer enhances the acidity of the particles and as a result improves their photocatalytic activity for the degradation of methylene blue significantly compared to commercial P25- $TiO_2$ . Presence of crystalline  $WO_3$  as a separate phase or reduced  $WO_x$  species though increases the adsorption of methylene blue and the resultant catalytic performance is poor. It is proven in the present study that, at a given concentration of  $WO_3$ , the density and the quality (Brønsted vs. Lewis) of surface acid sites and therewith the adsorption of a reactant/pollutant at the nanomaterial and its catalytic performance can be influenced by varying the process parameters of the FSS, which has not been reported to date.

#### Acknowledgements

The authors would like to acknowledge the EC and the Swiss BBW for their support of the FP5-Project Photocoat (EU Contract No. G5RD-CT-2002-00861; BBW Project No. 01.0571-1).

## References

- [1] J.-M. Herrmann, J. Disdier, J. Catal. Today 56 (2000) 389–401.
- [2] S. Djerad, L. Tifouti, M. Crocoll, W. Weisweiler, J. Mol. Catal. A: Chem. 208 (2004) 257–265.
- [3] S.T. Choo, S.D. Yim, I.-S. Nam, S.-W. Ham, J.-B. Lee, Appl. Catal. B: Environ. 44 (2003) 237–252.
- [4] T. Watanabe, S. Fukayama, M. Miyauchi, A. Fujishima, K. Hashimoto, J. Sol-Gel Sci. Technol. 19 (2000) 71–76.
- [5] P.V. Kamat, Chem. Rev. 93 (1993) 267–300.
- [6] A. Hagfeldt, M. Graetzel, Chem. Rev. 95 (1995) 49–68.
- [7] A.L. Linsebigler, G. Lu, J.T. Yates, Chem. Rev. 95 (1995) 735–758.
- [8] M.R. Hoffmann, S.T. Martin, W. Choi, D.W. Bahnemann, Chem. Rev. 95 (1995) 69–96.
- [9] M.A. Fox, M.T. Dulay, Chem. Rev. 93 (1993) 341–357.
- [10] T. Hirakawa, P.V. Kamat, Langmuir 20 (2004) 5645–5647.
- [11] M. Jakob, H. Levanon, P.V. Kamat, Nano Lett. 3 (2003) 353–358.
- [12] T. Johannessen, S. Koutsopoulos, J. Catal. 205 (2002) 404–408.
- [13] T. Sano, S. Kutsuna, N. Negishi, K. Takeuchi, J. Mol. Catal. A: Chem. 189 (2002) 263–270.
- [14] K. Vinodgopal, I. Bedja, P.V. Kamat, Chem. Mater. 8 (1996) 2180–2187.
- [15] K.K. Akurati, A. Vital, R. Hany, B. Bommer, T. Graule, M. Winterer, Int. J. Photoenergy 7 (2005) 153–161.
- [16] B. Pal, T. Hata, K. Goto, G. Nogami, J. Mol. Catal. A: Gen. 169 (2001) 147–155.
- [17] L. Spanhel, H. Weller, A. Henglein, J. Am. Chem. Soc. 109 (1987) 6632–6635.
- [18] Y.T. Kwon, K.Y. Song, W.I. Lee, G.J. Choi, Y.R. Do, J. Catal. 191 (2000) 192–199.
- [19] X.Z. Li, F.B. Li, C.L. Yang, W.K. Ge, J. Photochem. Photobiol. A: Chem. 141 (2001) 209–217.
- [20] H. Yang, R. Shi, K. Zhang, Y. Hu, A. Tang, X. Li, J. Alloys Compd. 398 (2005) 200–202.
- [21] C. Shifu, C. Lei, G. Shen, C. Gengyu, Powder Technol. 160 (2005) 198–202.
- [22] Y.R. Do, W. Lee, K. Dwight, A. Wold, J. Solid State Chem. 108 (1994) 198–201.
- [23] K.Y. Song, M.K. Park, Y.T. Kwon, H.W. Lee, W.J. Chung, W.I. Lee, Chem. Mater. 13 (2001) 2349–2355.
- [24] J. Engweiler, J. Harf, A. Baiker, J. Catal. 159 (1996) 259–269.
- [25] A. Rampaul, I.P. Parkin, S.A. O'Neill, J. DeSouza, A. Mills, N. Elliott, Polyhedron 22 (2003) 35–44.
- [26] T. Tatsuma, S. Takeda, S. Saitoh, Y. Ohko, A. Fujishima, Electrochem. Commun. 5 (2003) 793–796.
- [27] R. Mueller, L. Maedler, S.E. Pratsinis, Chem. Eng. Sci. 58 (2003) 1969–1976.
- [28] K. Wegner, S.E. Pratsinis, AIChE J. 49 (2003) 1667–1675.
- [29] R. Mueller, H.K. Kammler, S.E. Pratsinis, A. Vital, G. Beaucage, P. Burtcher, Powder Technol. 140 (2004) 40–48.
- [30] R. Mueller, R. Jossen, H.K. Kammler, S.E. Pratsinis, AIChE J. 50 (2004) 3085–3094.
- [31] L. Maedler, S.E. Pratsinis, J. Am. Ceram. Soc. 85 (2002) 1713–1718.
- [32] G. Ramis, G. Busca, C. Cristiani, L. Lietti, P. Forzatti, F. Bregani, Langmuir 8 (1992) 1744–1749.
- [33] H. Yang, D. Zhang, L. Wang, Mater. Lett. 57 (2002) 674–678.
- [34] T. Tani, N. Watanabe, K. Takatori, S.E. Pratsinis, J. Am. Ceram. Soc. 86 (2003) 898–904.
- [35] Y. Suyama, A. Kato, Ceram. Int. 8 (1982) 17–21.
- [36] R. Jossen, S.E. Pratsinis, W.J. Stark, L. Maedler, J. Am. Ceram. Soc. 88 (2005) 1388–1393.
- [37] M.A. Vuurman, I.E. Wachs, A.M. Hirt, J. Phys. Chem. 95 (1991) 9928–9937.
- [38] H. Habazaki, Y. Hayashi, H. Konno, Electrochim. Acta 47 (2002) 4181–4188.
- [39] J.H. Pan, W.I. Lee, Chem. Mater. 18 (2006) 847–853.
- [40] J.A. Horsley, I.E. Wachs, J.M. Brown, G.H. Via, F.D. Hardcastle, J. Phys. Chem. 91 (1987) 4014–4020.
- [41] G.C. Bond, S. Flamerz, L.V. Wijk, Catal. Today 1 (1987) 229–243.
- [42] S.S. Chan, I.E. Wachs, L.L. Murrell, L. Wang, W.K. Hall, J. Phys. Chem. 88 (1984) 5831–5835.
- [43] R. Zhang, J. Jagiello, J.F. Hu, Z.-Q. Huang, J.A. Schwarz, Appl. Catal. A: Gen. 84 (1992) 123–139.
- [44] C. Morterra, G. Ghiotti, E. Garrone, E. Fiescaro, J. C. S. Faraday T. 76 (1980) 2102–2113.
- [45] A. Gutiérrez-Alejandre, J. Ramírez, G. Busca, Langmuir 14 (1998) 630–639.
- [46] A. Gutiérrez-Alejandre, P. Castillo, J. Ramírez, G. Ramis, G. Busca, Appl. Catal. A: Gen. 216 (2001) 181–194.
- [47] F. Hilbrig, H.E. Goebel, H. Knoezinger, H. Schmelz, B. Lengeier, J. Phys. Chem. 95 (1991) 6973–6978.
- [48] H. Kominami, H. Kumamoto, Y. Kera, B. Ohtani, J. Photochem. Photobiol. A: Chem. 160 (2003) 99–104.
- [49] J.-M. Herrmann, Catal. Today 53 (1999) 115–129.
- [50] G. Rothenberger, J. Moser, M. Graetzel, N. Serpone, D.V. Sharma, J. Am. Chem. Soc. 107 (1985) 8054–8059.
- [51] H. Gerischer, A. Heller, J. Phys. Chem. 95 (1991) 5261–5267.
- [52] T. Yamanaka, K. Tanabe, J. Phys. Chem. 80 (1976) 1723–1727.